Materials Chemistry and Physics 181 (2016) 301–311

Contents lists available at ScienceDirect

Materials Chemistry and Physics

journal homepage: www.elsevier.com/locate/matchemphys

Synthesis and characterization of ^{159}Gd-doped hydroxyapatite nanorods for bioapplications as theranostic systems

Marcelo F. Cipreste, Anderson M. Peres, Alexandre A.C. Cotta, Fermin H. Aragón, Alan de M. Antunes, Alexandre S. Leal, Waldemar A.A. Macedo, Edésia M.B. de Sousa*

Centro de Desenvolvimento da Tecnologia Nuclear, CDTN, 31270-901 Belo Horizonte, MG, Brazil

HIGHLIGHTS

- Gd- HA nanorods were synthesized aiming their use as theranostic system.
- Gd^{3+} ions are trapped in the HA nanorods crystal net showing great stability.
- Gd- HA presents paramagnetic behavior indicating their use as contrast agents.
- HA-^{159}Gd-^{32}P were successful produced by neutron activation to act as a theranostic system.

ARTICLE INFO

Article history:
Received 30 December 2015
Received in revised form
18 May 2016
Accepted 17 June 2016
Available online 23 June 2016

Keywords:
Hydroxyapatite nanorods
Gadolinium
Neutron activation
Theranostic system

ABSTRACT

Gadolinium-doped hydroxyapatite (HA-Gd) nanorods have become promisor theranostic nanoparticles for early stage cancers as radioisotope carriers able to act in the treatment and multi-imaging diagnosis by single photon emission computed tomography and magnetic resonance imaging systems. In this work, gadolinium-doped HA nanorods were synthesized aiming the use as theranostic system for osteosarcomas. The as-prepared HA-Gd nanorods were characterized by XRD with Rietveld refinement method, FTIR, XPS, ICP-AES, TEM, SEM, BET and VSM in order to investigate the physical-chemical, morphology, pore size distribution and magnetic properties. Moreover, phosphorous and gadolinium in the HA-Gd sample were activated by neutron capture, in a nuclear reactor, producing ^{32}P and ^{159}Gd radioisotopes, and the surfaces of these nanorods were functionalized with folic acid. The results indicate that Gd^{3+} are trapped in the HA nanorods crystal net showing great stability of the HA-Gd interaction. Gadolinium provide paramagnetic properties on HA nanorods and structural phosphorous and gadolinium can be activated to induced gamma and beta activity. The well succeeded production of ^{159}Gd-^{32}P-HA makes this material a promisor agent to act as a theranostic system.

1. Introduction

Theranostic nanoparticles have received much attention of the world scientific community because these materials can spontaneously and selectively accumulate in specific tumor sites to promote the diagnose and treatment of cancer simultaneously [1,2]. Nanoscale theranostics usually refers to nano-agents with integrated imaging and therapy functions within a single nanoparticle systems [3]. Theranostic nanosystems are also multifunctional agents capable to combine passive and active targeting, environmentally-responsive drug release, molecular imaging and other therapeutic functions into a single platform [2]. These features are very interesting for cancer treatment due to the non-invasive and selective approach.

Bionanomaterials such as hydroxyapatite (HA) nanorods have become promisors theranostic agents for cancers in the early stage as magnetic-radioisotope carries due to their important characteristics such as nonimmunogenicity, biocompatibility, bioactivity and high osteoinductivity [4,5]. It is well demonstrated in the literature that HA nanorods can be synthesized through different methods [6–12] and these nanorods can easily adhere on osteosarcoma and osteoblast cells, promoting osteoblast growth and osteosarcoma cells uptake [13], making possible to use these nanorods as magnetic-radioisotope carriers targeting osteosarcomas in order to act in early imaging diagnosis systems and

* Corresponding author.
E-mail address: sousaem@cdtn.br (E.M.B. de Sousa).

http://dx.doi.org/10.1016/j.matchemphys.2016.06.063
0254-0584/

simultaneous radiotherapy treatment, in addition to the promotion of bone regeneration after tumor death. Moreover, apatite structures present high stability and flexibility, allowing some transition metal or lanthanide cation to be added as dopants in the apatite crystal lattice [14–18]. Jie Pan and colleagues [19] described a fabrication of a magnetic nanocomposite of fluoridate Ln^{3+}-doped HA and iron oxides with further biocompatible polymeric encapsulation showing excellent photoluminescence, magnetic properties and stability in aqueous solutions. Want et al. [20] described the development of Eu^{3+}-doped HA nanorods loaded with TPGS-FOL micelles presenting improved dispersion, high stability and excellent fluorescent property in aqueous solution. Both of these works demonstrate that the doping process of hydroxyapatite nanorods can improve their properties for biological applications.

Gadolinium is a paramagnetic lanthanide element already used in chelates working as a contrast medium agent for magnetic resonance imaging (MRI) systems [21–23]. This element enhances MRI images primarily by decreasing T1 relaxation constant of the tissues in which it localizes [21,24]. An important feature of gadolinium is that it can be activated in a nuclear reactor to produce the radioisotope ^{159}Gd, a beta and gamma radiations emitter [25]. This radionuclide can be able to act in multi-imaging diagnosis on single photon emission computed tomography (SPECT) and MRI systems. However, there is a recent concern that gadolinium, as a free ion, is extremely toxic when dissociated from its chelate and deposited in tissues. Such limitations may affect the applicability of these materials as magnetic-radioisotope carriers [21].

In the other hand, the presence of folic acid in the nanoparticles surface promotes their delivery into specific cancer cells since its receptor is overexpressed in several human tumors [26,27]. In this direction gadolinium doped HA nanorods functionalized with folic acid could provide an efficient active targeting to osteosarcomas and promote the internalization of these nanorods in osteosarcoma cells. Thereby, HA can help to overcome problems encountered in the current methods of treatment and diagnosis of this tumor type [28,29].

In this study, gadolinium-doped HA nanorods (HA-Gd) were synthesized by hydrothermal co-precipitation method and the effect of gadolinium concentration on the crystal structure and physical-chemical properties of HA-Gd nanorods was investigated. To provide active targeting, HA-Gd nanorods were functionalized with folic acid. In next step, HA-Gd nanorods were evaluated for neutron activation in a nuclear reactor. So, the aim of present work was to produce gadolinium-doped hydroxyapatite nanorods functionalized with folic acid to act as a theranostic system with active targeting to osteosarcomas. The results indicates that this material can be used as contrast agents for MRI diagnosis and the well successfully production of HA-^{159}Gd-^{32}P by neutron activation makes this material even more promising to act as a theranostic system.

2. Materials and methods

2.1. Materials

The reagents calcium nitrate tetrahydrate ($Ca(NO_3)_2 \cdot 4H_2O$), potassium phosphate dibasic trihydrate ($K_2HPO_4 \cdot 3H_2O$), hexadecyltrimethylammonium bromide (CTAB), sodium hydroxide (NaOH), gadolinium chloride ($GdCl_3$), folic acid, dimethylsulfoxide (DMS), 1-ethyl-3-(3-dimethylaminopropyl) carbodiimide hydrochloride (EDC), N-hydroxysuccinimide (NHS), ethylenediamine and acetone, from Sigma-Aldrich, were used as received without further purification.

2.2. Synthesis of Gd-doped hydroxyapatite nanorods

Hydroxyapatite nanorods were prepared by surfactant-assisted hydrothermal method with some modifications of the methodology found in the literature [30,31]. The present method consisted in the preparation of two precursor solutions: (I) calcium and gadolinium and (II) phosphate. The preparation of solution (I) started with the complete dissolution of CTAB (2 g) in 150 mL Milli-Q® water to promote micelles formation, followed by dissolution of calcium nitrate tetrahydrate (0.167 M). This solution was kept under stirring for 5 h to promote self-assembly of calcium ions on the CTAB micelles; then gadolinium chloride was added in three concentrations of Gd (0, 1.3 and 2.8%, named as HA, HA-Gd1.3 and HA-Gd2.8 respectively) with respect to the atomic percentage of Ca^{2+}. Solution (II) was prepared by the complete dissolution of potassium phosphate dibasic trihydrate (0.1 M) in 150 mL Milli-Q® water. The pH of both solutions was adjusted to 12 with NaOH. Then, solution (II) was slowly added in the solution (I) using a motor-driven burette under vigorous stirring. The resultant suspension was kept under stirring overnight in a hydrothermal reactor during 10 h at 100 °C. The filtrated powder was dried during 24 h and calcined in tubular furnace at 600 °C during 6 h to promote CTAB removal, resulting in a fine white powder.

2.3. HA-Gd functionalization with folate

The functionalization method followed the amination process of folate described by Pan et al. [32] and Lee et al. [33]. Briefly, folic acid (FA) was dissolved in dimethylsulfoxide; 1-ethyl-3-(3-dimethylaminopropyl) carbodiimide hydrochloride and N-hydroxysuccinimide were added in the solution and stirring during 6 h at 50 °C. Ethylenediamine was added in this solution and allowed to react stirring overnight. This material was dried at room temperature during 24 h. The functionalization process of HA-Gd with aminated FA was carried out by mixing a 1:2 M proportion of HA-Gd2.8 and aminated folate in Milli-Q® water and keeping under vigorous stirring during 24 h at 50 °C. The resulting yellow powder (FA/HA-Gd2.8) was washed with acetone and Milli-Q® water under vacuum filtration system and then was dried at room temperature during 24 h.

2.4. Characterization

The crystalline phases of the sample were evaluated by X-ray diffraction (XRD - Rigaku Inc., Japan) with Cu Kα radiation ($\lambda = 0.154$ nm) in which data were collected from 10° to 80° (2θ) with a step size of 1°/min in order to perform the Rietveld refinement. Fourier transform infrared spectra (FTIR - Nicolet 6700, Thermo Scientific, USA) were recorded in the range of 4000–400 cm^{-1} and 64 scans to evaluate the chemical composition of the samples prepared in KBr (Sigma-Aldrich) powder. Particle size and morphology analyses were evaluated by transmission electron microscopy (TEM - Tecnai G2-12 SpiritBiotwin, FEI Company, USA) and scanning electron microscopy (SEM – Σigma VD series, ZEISS, Germany). The porosity parameters and nitrogen adsorption isotherms of samples were obtained at 77 K using a Quantachrome Autosorb iQ adsorption analyzer (Quantachrome, EUA); the samples were outgassed during 2 h at 300 °C. All data analyses were performed using the Quantachrome Instruments software (Boynton Beach, FL, USA). Magnetic characteristics of the samples were performed by vibrational sample magnetometry (VSM – 7400 series, LakeShore Cryotronics, USA). X-ray photoelectron spectroscopy analysis (XPS – Specs, Phoibos-150 electron analyzer) was carried out to investigate the surface interactions between HA, Gd and FA, using monochromatized Al Kα radiation

(1486.6 eV) at a power of 350 W. An electron flood gun, operated at 0.1 μA, was used to compensate the charge effects in the samples. The C 1s signal (284.6 eV) was used as reference for the calibration of the binding energies (BE) of different elements.

2.5. HA-Gd interaction stability assay

The stability of the chemical interactions between hydroxyapatite constituents and gadolinium was investigated in aqueous suspensions at different time intervals. This assay consisted in the preparation of 1 mg/mL of HA-Gd2.8 (pH 7) suspensions that were incubated and kept stirred at 37 °C during variable time intervals (2, 6, 8, 24 and 56 h). After each incubation time, the suspensions were filtrated and the passing liquid was analyzed by inductively couple plasma – atomic emission spectrometry (ICP-AES – Spectroflame, Spectro Analytical Instruments, Germany) to evaluate the Gd content that could be released from HA matrix.

2.6. Neutron activation of structural phosphorous and gadolinium

The production of ^{32}P and ^{159}Gd radioisotopes occurred by the irradiation of HA and HA-Gd2.8 samples in TRIGA Mark-1 100 kW nuclear research reactor sited on CDTN (Belo Horizonte, Brazil). 62 mg of HA and HA-Gd2.8 samples were irradiated during 4 h under a thermal neutron flux of 6.4×10^{11} cm^{-2} s^{-1}. In order to investigate the phosphorous activation, $^{31}P(n,\gamma)^{32}P$, beta spectroscopy measurements in HA sample were performed in a beta counter (Thermo Eberline HandECount, Thermo Electron Corporation, USA). To analyze the gadolinium activation, $^{158}Gd(n,\gamma)^{159}Gd$, the gamma spectrum of the irradiated HA-Gd2.8 was obtained using a HP-Ge detector with nominal efficiency of 50% and the Canberra Genie 2000 software [34].

2.7. Colloidal stability assay

The colloidal stability of the nanorods was evaluated through the monitoring zeta potential values of the samples during 7 days. The analytical procedure was carried out in a Zetasizer Nano Zs (Malvern, USA). The samples were prepared at concentration of 10 μg/mL dispersed in 0.5 M NaCl with a conductivity of approximately 120 ± 20 mS/cm^2.

3. Results and discussions

3.1. X-ray diffraction

X-ray diffraction patterns of HA, HA-Gd1.3 and HA-Gd2.8 nanorods were obtained at room temperature and the results are presented in Fig. 1(a), (b) and (c). For all these samples, the diffraction peaks can be indexed to the hexagonal phase with space group $P6_3/m$ (JCPDS card 9-432). Additional crystalline or amorphous phases were not observed within the limit of detection of our measurements. The Rietveld refinements of XRD patterns were carried out and the results for the lattice parameters (*a, c*), unit cell volume (*V*) and mean grain size (<*D*>) are summarized in Table 1, respectively. Fig 1(d) shows the dependence of the volume in function of the Gd-content. The peak shapes were modeled by using a Lorentzian-type function within the General Structure Analyses System (GSAS) software program [35] and the calculated atomic positions were used to mount the undoped HA unit cell (Fig. 2) where it is possible to localize the Ca^{2+} and PO_4^{3-} ions positions on the lattice. The calcium ions occupy two typical positions, Ca(1) and Ca(2), as expected. The calculated unit cell volume for the undoped HA sample (526.44 Å^3, Table 1) is slightly smaller when compared with the literature (529.84 Å^3) [36], possibly due to the small mean grain size. On the other hand, when the doping is carried out, the unit cell volume of HA-Gd1.3 and HA-Gd2.8 samples show progressive increases (Fig. 1(d)) that could be attributed to the entry of the Gd^{3+} ions on the lattice because the hydroxyapatite structure is open and can host cations in the Ca^{2+} sites or in the interstice positions [37]. Likewise, the Fourier maps (Fig. 3) of the undoped HA and HA-Gd2.8 samples exhibit differences on the electronic density surrounding the Ca^{2+} ions on Ca(2) sites; this may be an evidence of the substitution of gadolinium ions in these positions.

The mean grain sizes were estimated using the Scherrer's relation: $<D> = K\lambda/\beta_{Size}cos\theta$, where $K = 0.9$ for spherical shape, λ is the radiation wavelength (1.5418 Å for *Cu* K_α), β_{Size} is the size contribution to full width at half-maximum (*FWHM*) of the reflection peaks, and θ is the diffraction angle. The mean size values decrease as the nominal Gd-content increases, and this is an important effect of the doping process, already observed in others doped HA nanoparticulated systems [38].

3.2. Fourier transform infrared spectroscopy

The FTIR spectra were obtained to investigate the chemical composition of the hydroxyapatite samples doped with gadolinium (Fig. 4). All the samples exhibit transmittance bands related to the characteristic vibrational modes of HA [39–42]. The weak shoulder at 961 cm^{-1} and strong broad band at 1036 cm^{-1} correspond to ν_1 and ν_3 stretch vibrational modes of phosphate group while the shoulder at 473 cm^{-1} and the strong bands at 565 and 604 cm^{-1} indicate the presence of the ν_2 and ν_4 bending vibrational modes of the same group. The bands relating to the stretch of the OH group can be observed at 3569 and 631 cm^{-1}. The broad band observed from 3237 to 3663 cm^{-1} could be attributed to vibrational modes of water, likewise the weak band around 1649 cm^{-1} [43].

The double bands at 1418 and 1479 cm^{-1}, observed only in the undoped sample, may be attributed to the presence of CO_3^{2-}, suggesting the formation of carbonated hydroxyapatite [41,42]. Carbonate ions can substitute either the phosphate group (type B) or the hydroxyl group (type A) in HA lattice [44]. The B-type carbonated HA can be precipitated from solutions in temperature range of 50–100 °C [45]. As the synthesis was carried out at room temperature and the hydrothermal treatment at 100 °C, it is reasonable to assume that B-type carbonated HA was formed and the CO_3^{2-} ions substitution could be occur due to the samples exposure to atmospheric CO_2 before the hydrothermal treatment. A second possibility suggests CTAB decomposition during hydrothermal treatment.

The reactant used as gadolinium source, $GdCl_3$, exhibits an intense transmittance band at 1402 cm^{-1} attributed to the Gd–Cl interactions. This band can shifted to 1382 cm^{-1} for doped samples resulting in a chemical interaction between Gd^{3+} and PO_4^{3-} [46]. Our proposal is that gadolinium ions substitute calcium in the lattice, as indicated by XRD analyses, resulting in strong interactions with phosphate and inhibiting the carbonate formation. In the case of this sample it can be observed an inhibition of the carbonate formation in the Gd-doped HA nanorods. This behavior could be explained through an interaction between Gd^{3+} – PO_4^{3-} within the HA-Gd crystal that possibly will have created a stronger linkage between these two ions, making difficult the carbonate ions diffuse inside the nanorods.

3.3. Scanning and transmission electron microscopy

SEM images were taken in order to investigate the influence of gadolinium on the shape and particle size distribution of HA-Gd samples. As it could be seen at the rod shape was not altered by

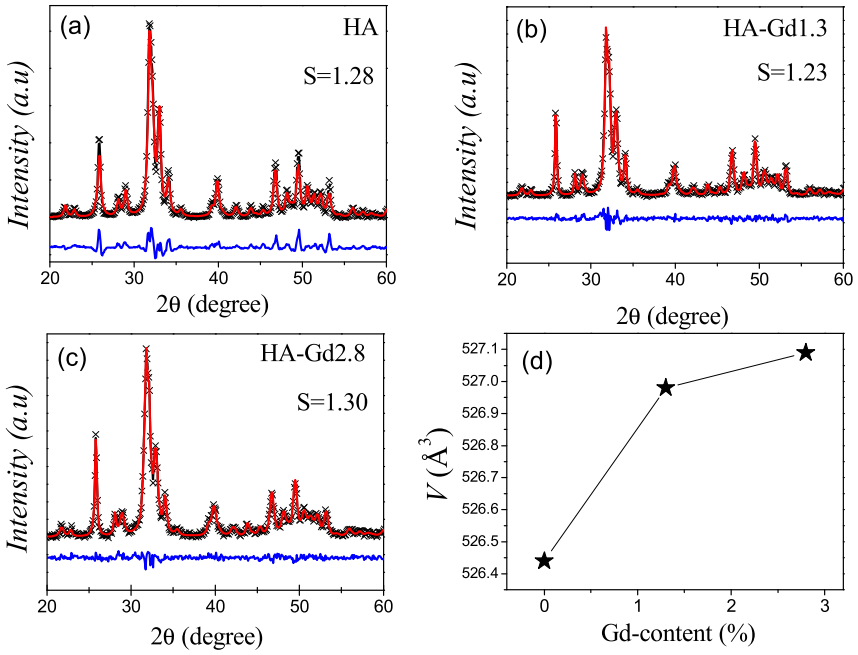

Fig. 1. Diffraction patterns with Rietveld refinement of the (a) HA, (b) FA-Gd1.3 and (c) HA-Gd2.8 samples. The observed and calculated data are represented by the stars and solid lines, respectively. Differences between observed and calculated data are also shown. The quality of the refinements is represented by the S values. (d) Dependence of the volume as a function of the Gd content.

Table 1
Parameters obtained from the Rietveld refinement of XRD: The mean grain size (<D>), lattice parameters (*a*, *c* and V) and S = R-exp/R-wp, parameter that quantifies the quality of the refinement.

Sample	*a* (Å)	*c* (Å)	*V* (Å^3)	<*D*> (nm)	S (−)
Bulk [36]	9.4300	6.8800	529.84	–	–
HA	9.3971	6.8838	526.44	26 (2)	1.28
HA-Gd1.3	9.4005	6.8859	526.98	24 (2)	1.23
HA-Gd2.8	9.4038	6.8824	527.09	18 (2)	1.30

the presence of Gd in the synthesis although the particle size distribution is slightly modified (Fig. 5(d)), in agreement with the XRD results. TEM images of the HA sample confirm a rod morphology of nanoparticles [Fig. 6(a) and (b)]. Through high resolution TEM images [Fig. 6(c) and (d)] it is possible to observe that nanorods are constituted of smaller crystallites, and the 002 interplanar distance of about 0.34 nm was measured in agreement with the literature [14]. All the measurements realized in TEM and SEM images were performed through the Quantikov Image Analyzer software [47].

3.4. Nitrogen adsorption analysis

N_2 adsorption analyzes allowed to investigate the influence of gadolinium on the surface area and porosity of the hydroxyapatite nanorods. HA sample shows type IV isotherm with H3 hysteresis loop [48], as it can be seen on Fig. 7. The addition of gadolinium to the synthesis process does not change the isotherm form neither the hysteresis loop, but the adsorbed N_2 volume is higher for all the relative pressures in the Gd-doped samples. The inserted table on Fig. 7 presents the textural characteristics of the samples, showing that the surface area, pore volume and pore diameter became higher for doped samples (49 m^2/g to 66 m^2/g and 81 m^2/g;

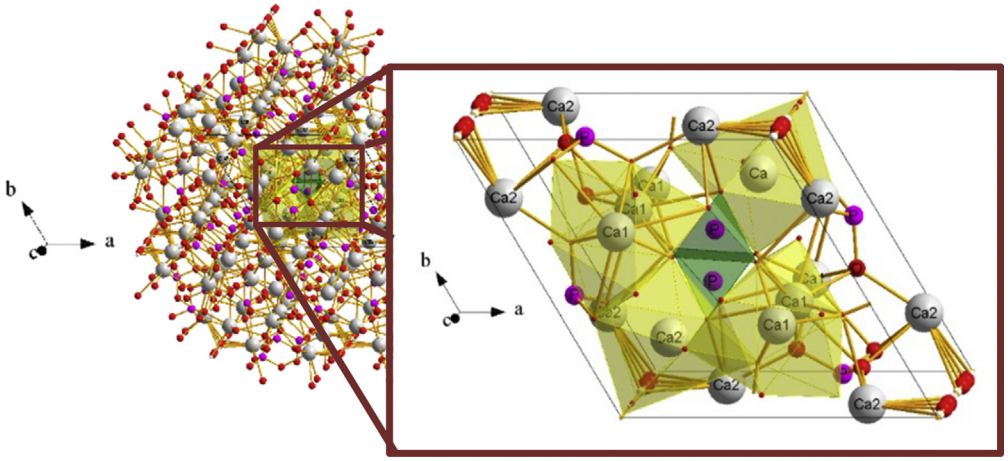

Fig. 2. Unit cell of the hydroxyapatite structure, where are observed the Ca, P, O and H sites (silver, pink, red and white respectively). (For interpretation of the references to colour in this figure legend, the reader is referred to the web version of this article.)

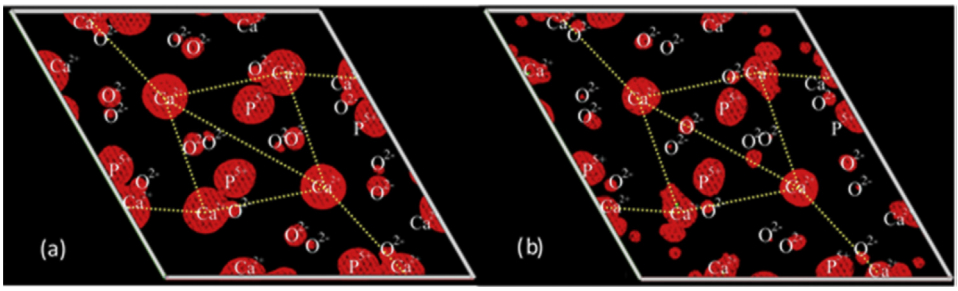

Fig. 3. Fourier difference map to the undoped HA and HA-Gd2.8% samples.

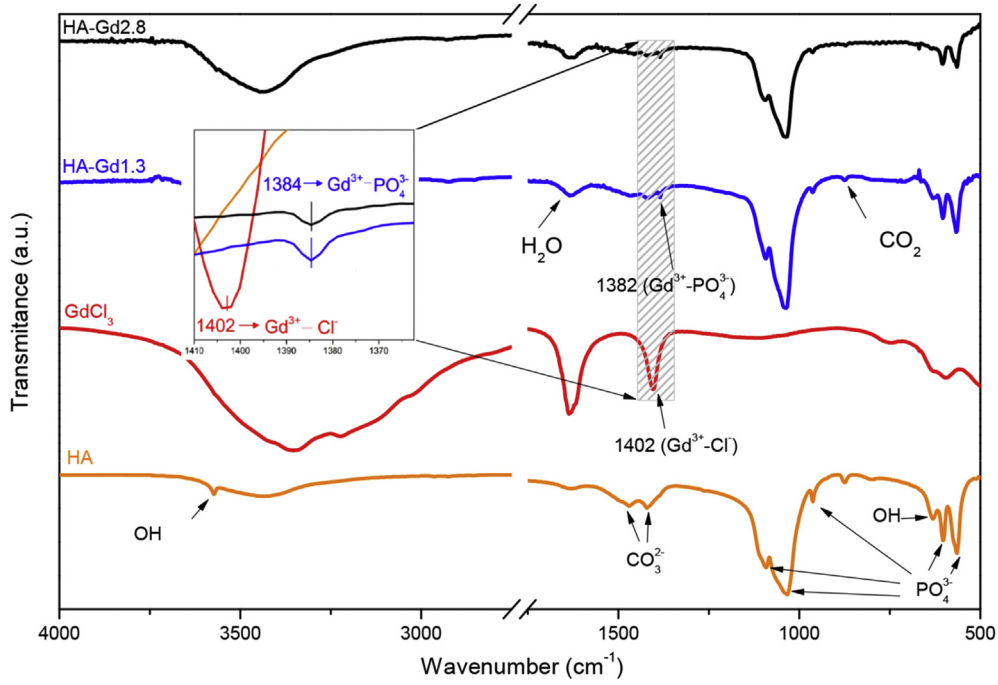

Fig. 4. FTIR spectra of the samples with an inset where it is possible to observe the shift attributed to Gd interactions.

0.09 cm^3/g to 0.51 cm^3/g and 0.34 cm^3/g; 18 nm–31 nm and 32 nm, respectively), suggesting that gadolinium modifies the formation of CTAB micelles before the nucleation of HA crystals starts. Similar features are also found for other ceramics doped with metals [49,50]. The increased pore volume and diameter are important features that make the HA-Gd nanorods promisor candidates to act as drug delivery systems, allowing the simultaneous employment of some chemical radiosensitizers as a multimodal therapy strategy in the theranostic system proposed in the present work [51–55]. The increased surface area favors the functionalization process of the nanorods with different organic molecules that make the nanostructures stealth in the bloodstream, avoiding the phagocyte system and providing active targeting to cancer cells [56].

3.5. X-ray photoelectron spectroscopy analysis

XPS analysis was carried out to evaluate the doping and functionalization processes. Three samples HA, HA-Gd2.8 and FA/HA-Gd2.8 were analyzed in order to perform a comparative study. The survey spectra of the samples are shown in Fig. 8(a). The hydroxyapatite nanorods surfaces are constituted only by Ca, P, O and C. In the spectra of the samples containing Gd, due to the use of Al Kα radiation and the low concentration of Gd, it is not possible to distinguish clearly the Gd 3d peaks from Ca LMM Auger transitions. For the FA/HA-Gd2.8 sample, the presence of folic acid at the surface is confirmed by the nitrogen peaks in the survey spectrum.

High resolution spectra of P 2p, O 1s and Ca 2p peaks of HA and HA-Gd2.8 are shown in Fig. 8(b), (c) and (d), respectively, and the binding energies are indicated in Table 2. In HA sample, phosphorus 2p 3/2 and 2p 1/2 peaks have binding energy of 133.8 eV and 134.6 eV, respectively, and they are assigned to P tetrahedrally coordinated to O [57,58]. The Ca 2p spectra have been deconvoluted into two doublets due to the spin-orbit splitting, corresponding to the two Ca sites, one in a columnar structure parallel to the *c* axis, named Ca(1), and another one in a triangular net around the OH group, named Ca(2). It should be pointed out that XPS measurements from the HA sample indicate also the presence of carbonate ions CO_3^{2-} (article under review), as mentioned in the FTIR results. The Ca 2p doublet peak with 346.6 eV and 350.2 eV have been attributed to Ca 2p 3/2 and 2p 1/2 at $CaCO_3$ [59] and Ca(2). Finally, in the O 1s spectrum from pure HA, three O specimens could be observed, with the peaks at 532.1 eV, 530.8 eV and 528.5 eV corresponding to O=P, O–P/O–Ca and hydroxyl OH surrounded by Ca, respectively [57].

The incorporation of gadolinium into hydroxyapatite can take place through the substitution of Ca(1) and Ca(2) by Gd atoms, or by

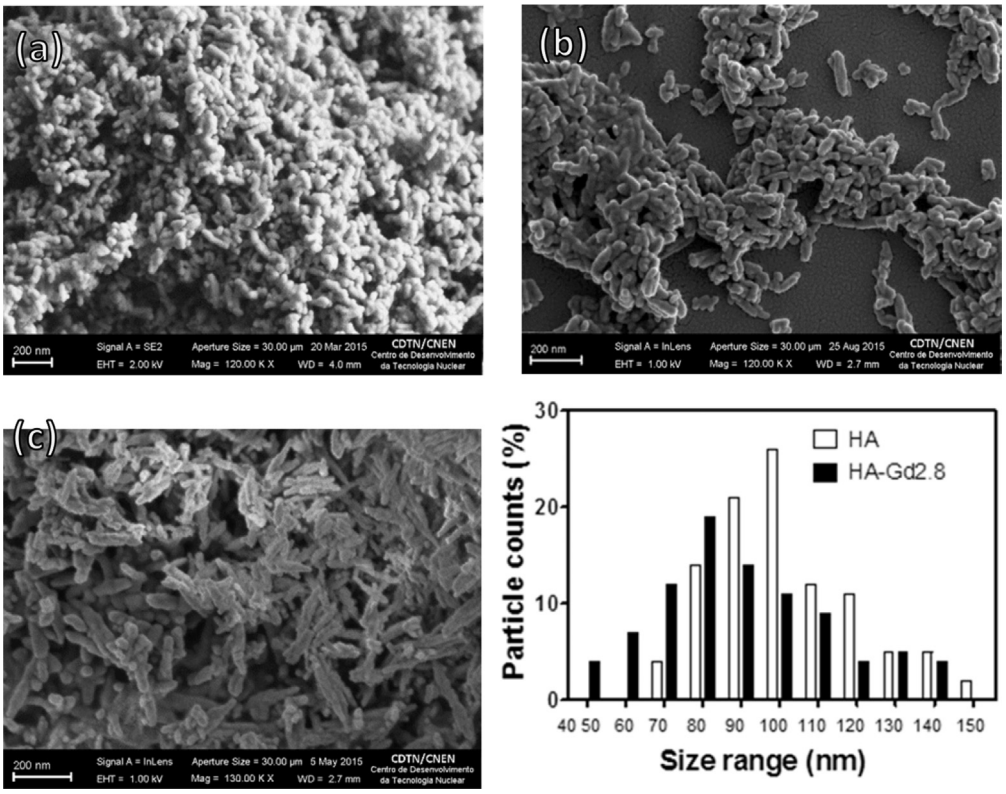

Fig. 5. SEM images of (a) HA, (b) HA-Gd1.3 and (c) HA-Gd2.8 and (d) particle size distribution chart.

Gd occupying interstitial sites. From the XPS measurements after the Gd^{3+} incorporation in HA, the intensity of the Ca 2p doublet originally attributed to $CaCO_3$ and Ca(2) with 346.6 eV and 350.2 eV at Ca 2p spectrum decrease significantly, as expected, since CO_3 depletion has been observed in the FTIR results. Furthermore, high resolution spectrum at O 1s region does not show the hydroxyl group too, as before. Since Gd^{3+} substitution at $Ca(2)^{2+}$ site should be followed by the replacement of OH^- by O^{2-} or by a cation vacancy for charge balance [60,61], the XPS results suggest the first mechanism for the Gd incorporation. A new peak at 536.9 eV is also observed in the O 1s spectrum and it is attributed to the presence of H_2O. Such behavior can be explained by the presence of Gd in the HA, once it has a strong hygroscopic character as it could also be seen in FTIR spectra. All other peaks at Ca 2p and of P 2p region appear shifted by around −1.0 eV when compared with pure HA, suggesting a chemical interaction between P and Gd, supporting the analysis of FTIR results.

After functionalization process, P 2p and Ca 2p peaks decrease their intensities, due to the presence of aminated folic acid at the surface, as shown at Fig. 9(a) and (b) respectively. Moreover, all these peaks are shifted again by around −1.0 eV, as also indicated in Table 2, possibly due to a new interaction between folic acid and HA-Gd surface, similar to the one observed in a previous work (article under review).

Thus, the XPS results, indicating the incorporation of Gd into HA by replacing Ca(2) sites, and the chemical shifts allow us to propose that the doping and functionalization processes were succeeded and Gd can be strongly bonded in HA matrix, in agreement with HA-Gd interaction stability assay showed next.

3.6. HA-Gd interaction stability assay

The ICP-AES results for the filtrated liquid of incubated HA-Gd2.8 suspensions revel that Gd is not released from HA matrix because no traces of Gd were found in the liquid phase, so the concentration of Gd is very small([Gd] > 0.01 mg/L), suggesting that this material retain gadolinium and reduce or eliminate the toxicity observed for the gadolinium-based contrast media currently available [21,62].

3.7. Vibrational sample magnetometry

VSM analyzes were performed to investigate the magnetic susceptibility of the Gd-doped hydroxyapatite. The hysteresis loops of the samples are shown on Fig. 10, revealing that the presence of gadolinium alters the magnetic behavior of hydroxyapatite nanorods from diamagnetic (undoped HA) to paramagnetic (Gd doped samples); these results were also found in similar works [63,64]. It should be pointed out that it is possible to incorporate larger atomic amount of Gd in such samples to provide higher magnetizations in the HA nanorods [64]. Considering the results obtained from XPS and HA-Gd interaction stability assay which indicate that Gd ions are not released from HA matrix, it is reasonable to assume that HA-Gd nanorods have potential applications as contrast agents for MRI, besides being used simultaneously as therapy functions.

3.8. Neutron activation of structural phosphorous and gadolinium

Two samples were investigated by neutron activation analysis: first, the undoped sample (HA) was irradiated in order to investigate only the activation of structural phosphorous of the hydroxyapatite nanorods, since ^{159}Gd is a beta emitter and the beta counter does not discriminate beta radiation from distinct radionuclides. Then, samples containing Gd ions (HA-Gd2.8) were irradiated to analyze ^{159}Gd. The results indicate that a specific activity of 7.8 kBq/mg due to phosphorous was induced in HA sample. The

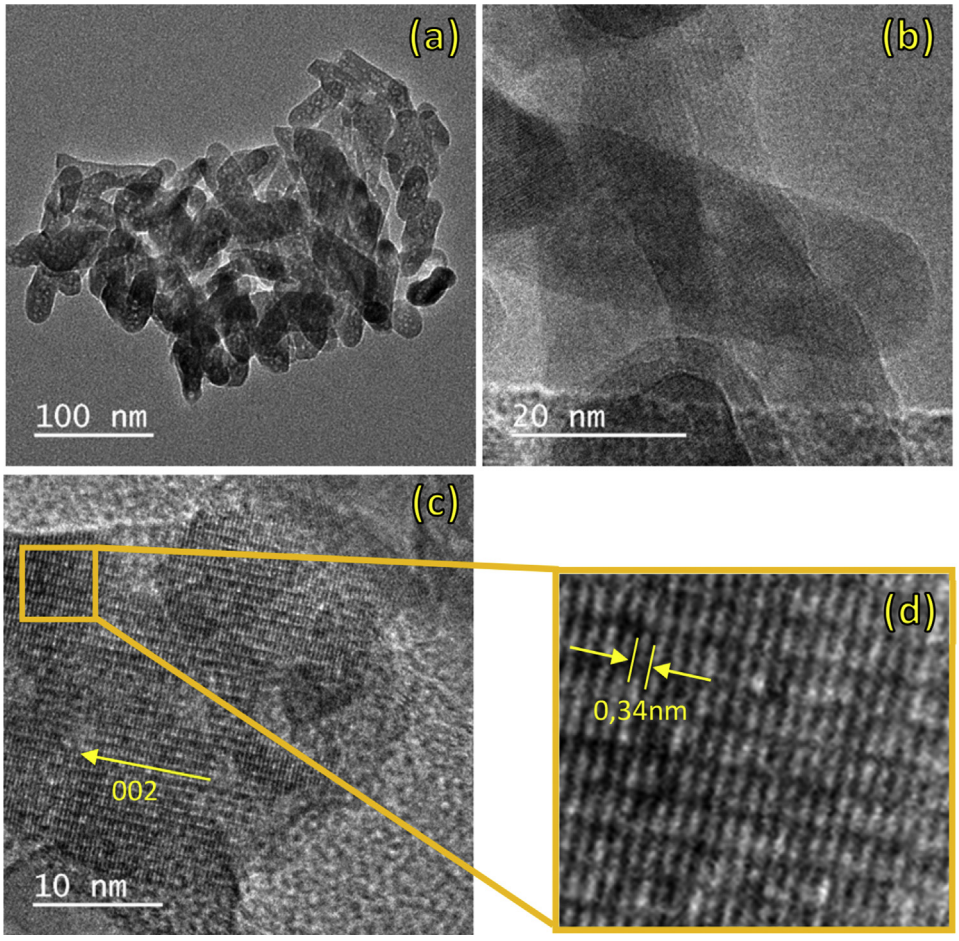

Fig. 6. TEM images of HA nanorods.

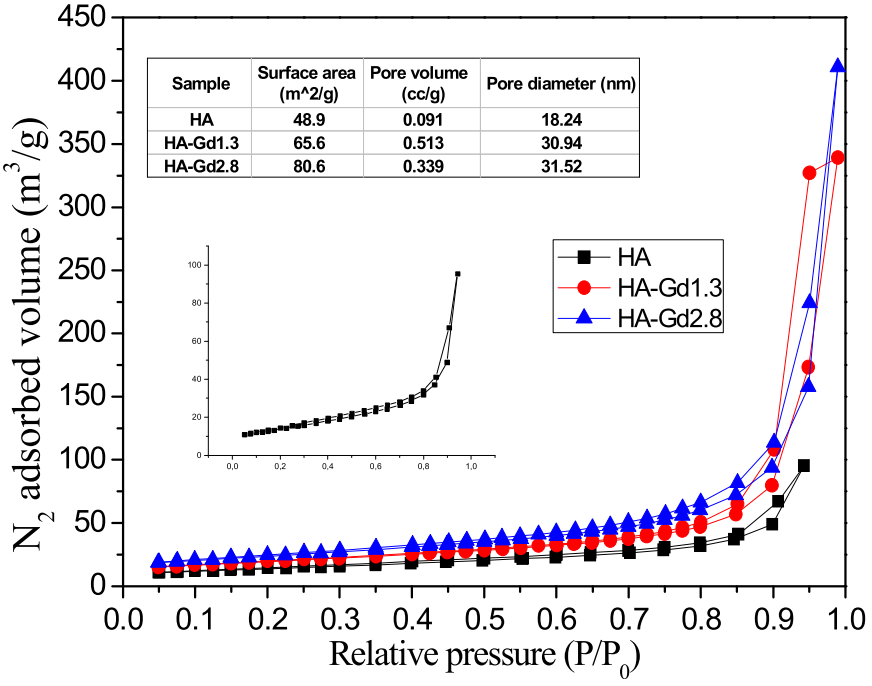

Fig. 7. N_2 adsorption isotherms and BET and BJH surface parameters of the samples.

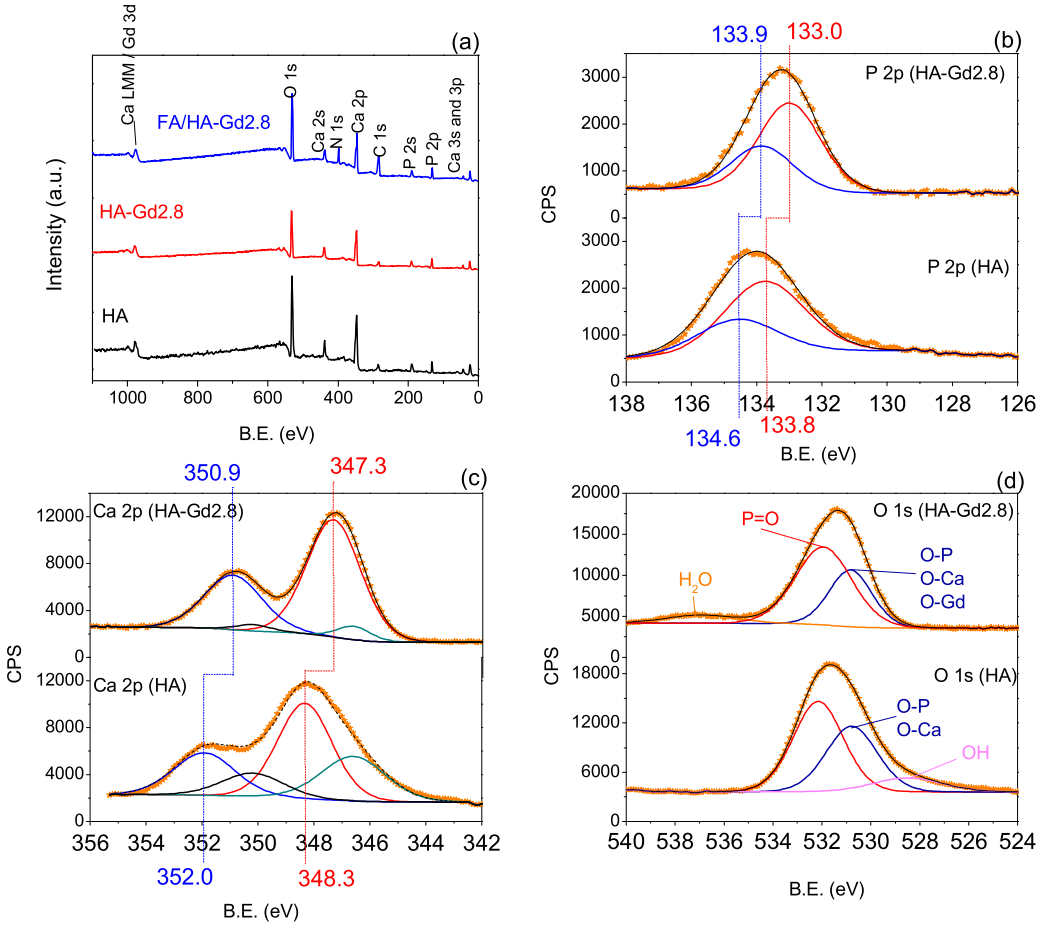

Fig. 8. (a) XPS survey spectra, (b) XPS high resolution spectra of P 2p, (c) XPS high resolution spectra of Ca 2p and (d) XPS high resolution spectra of O 1s for HA and HA-Gd2.8 samples. The background were subtracted in P 2p, Ca 2p and O 1s spectra.

Table 2
Surface elemental analysis of O, P and Ca species obtained by XPS.

	HA		HA-Gd2.8		FA/HA-Gd2.8	
	B.E.	%	B.E.	%	B.E.	%
O type						
O–P/O–Ca	530.8	37.9	530.8	32.8	530.42	35.8
O═P	532.1	51.2	531.9	59.7	531.67	35.4
Hydroxyl	528.5	10.9	nd	nd	529.4	28,8
H_2O	nd	nd	536.9	7.52	nd	nd
Ca type						
Ca(1) 2p 3/2	348.3	42.9	347.3	62.2	346.7	52.0
Ca(1) 2p 1/2	351.9	21.5	350.9	31.1	350.2	26.0
Ca(2) 2p 3/2	346.6	23.8	346.6	4.4	345.4	14.6
Ca(2) 2p 1/2	350.2	11.9	350.2	2.2	349.0	7.3
P type						
P 2p 3/2	133.8	66.7	133.0	66.7	131.8	66.7
P 2p 1/2	134.6	33.3	133.8	33.3	132.6	33.3

gamma spectrum of HA-Gd2.8 is shown in Fig. 11, in which the main photopeaks of ^{159}Gd can be found at 363.54 and 348.28 keV [65]. The induced gamma activity was 4.8 μCi in 62 mg of HA-Gd2.8. These results prove that the structural phosphorous and gadolinium can be activated in the gadolinium-doped hydroxyapatite nanorods to produce HA-^{159}Gd-^{32}P, making possible to obtain a stable theranostic system without a need of a posterior radioisotopic marking that leads to weak interaction between nanorods and radioisotopes. Thus, avoiding radioisotopes escaping from the HA structure, the tracking strategy of nanorods and the radiation delivery could be more specific in osteosarcomas due to the targeting provided by the functionalization with folic acid.

3.9. Colloidal stability assay

The physical stability was evaluated by Zeta potential parameters, using the dynamic light scattering technique for 7 days (pH = 7.0). At the same time, the phenomenon of sedimentation/creaming was evaluated in samples through visual control. The changes in the Zeta potential for all samples within the same period of time are illustrated in Fig. 12. No statistically significant variation could be observed in the zeta potentials for all the samples within the time period of 7 days. The Zeta potential can change the behavior of nanoparticles within in vivo environments, given that the presence of electrical charges can minimize agglomeration phenomena or drive the in vivo destiny of nanosystems. This preliminary study indicates that no physical degradation occurred on the samples, suggesting that the colloidal dispersion of these samples present stability and adequate features for biological applications.

4. Conclusions

In this work, gadolinium-doped (1.3 and 2.8%) HA nanorods were prepared and characterized in order to determine their potential application as theranostic system for osteosarcomas. The obtained results demonstrated that the formation and structural

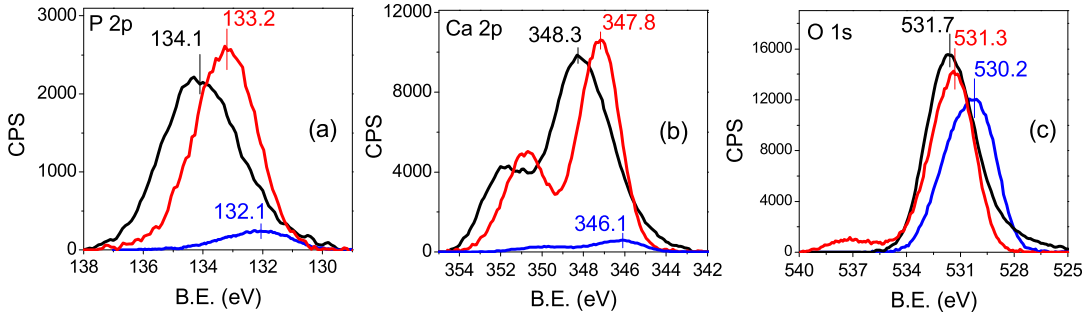

Fig. 9. High resolution XPS spectra of (a) P 2p, (b) Ca 2p and (c) O 1s for HA (black), HA-Gd2.8 (red) and FA/HA-Gd2.8 (blue) samples. (For interpretation of the references to colour in this figure legend, the reader is referred to the web version of this article.)

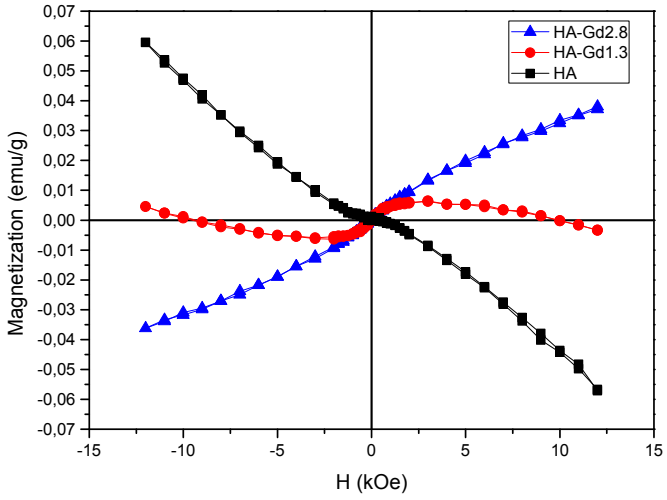

Fig. 10. VSM hysteresis loops showing that gadolinium ions can alter the magnetic behavior of HA from diamagnetic (undoped HA) to paramagnetic (HA-Gd samples).

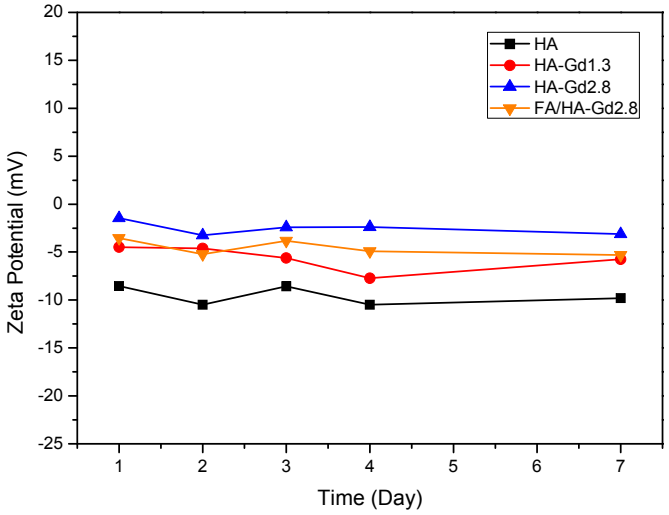

Fig. 12. Changes in zeta potential as a function of time.

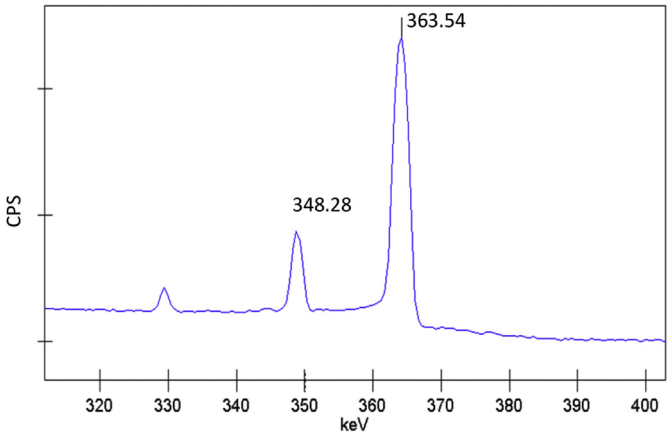

Fig. 11. Gamma spectra of the activated HA-Gd2.8 and the photopeak of ^{159}Gd.

features of HA-Gd were influenced by incorporation of different Gd content. Based on the XRD results, the unit cell volume increases as the nominal Gd-content increases, indicating that Gd ions can be trapped on HA lattice in the interstice or by substitution on Ca sites, showing great stability of the HA-Gd interaction with no release of gadolinium to environment. SEM and TEM images showed that all samples presented nanorod shape and the size distribution is relatively narrow. It was also demonstrated by the present study that the paramagnetic behavior of gadolinium-doped hydroxyapatite is really due to final product and not from released Gd ions, indicating that these materials can be used as contrast agents for MRI diagnosis. The successful production of HA-^{159}Gd-^{32}P by neutron activation makes this material even more promising to act as a theranostic system. Furthermore, the increased porosity of the nanorods allows to conjugate radiotherapy and chemotherapy throughout the incorporation of radiosensitizer drugs inside the mesoporous structure, making possible to reduce the radioresistance of osteosarcoma. Likewise, the functionalization of the HA-Gd nanorods with folic acid can provide active targeting to osteosarcomas, crediting this nanorods for extensive biological assays in order to study the efficiency of this system to accumulate selectively into the osteosarcoma cells, to promote the treatment of tumor and stimulate bone regeneration after the treatment.

Acknowledgments

This research was supported by the Brazilian agencies CAPES, CNPq and FAPEMIG. The authors would like to thank the Microscopy Center - UFMG for technical support during electron microscopy work.

References

[1] R. Bardhan, S. Lal, A. Joshi, N.J. Halas, Theranostic nanoshells: from probe design to imaging and treatment of cancer, Acc. Chem. Res. 44 (2011) 936–946, http://dx.doi.org/10.1021/ar200023x.

[2] S.M. Janib, A.S. Moses, J.A. MacKay, Imaging and drug delivery using theranostic nanoparticles, Adv. Drug Deliv. Rev. 62 (2010) 1052–1063, http://dx.doi.org/10.1016/j.addr.2010.08.004.
[3] Q. Chen, H. Ke, Z. Dai, Z. Liu, Nanoscale theranostics for physical stimulus-responsive cancer therapies, Biomaterials 73 (2015) 214–230, http://dx.doi.org/10.1016/j.biomaterials.2015.09.018.
[4] D. Yamini, G. Devanand Venkatasubbu, J. Kumar, V. Ramakrishnan, Raman scattering studies on PEG functionalized hydroxyapatite nanoparticles, Spectrochim. Acta - Part A Mol. Biomol. Spectrosc. 117 (2014) 299–303, http://dx.doi.org/10.1016/j.saa.2013.07.064.
[5] W. Pon-On, N. Charoenphandhu, J. Teerapornpuntakit, J. Thongbunchoo, N. Krishnamra, I.M. Tang, Physicochemical and biochemical properties of iron-loaded silicon substituted hydroxyapatite (FeSiHAp), Mater. Chem. Phys. 141 (2013) 850–860, http://dx.doi.org/10.1016/j.matchemphys.2013.06.014.
[6] X.-Y. Zhao, Y.-J. Zhu, B.-Q. Lu, F. Chen, C. Qi, J. Zhao, et al., Hydrothermal synthesis of hydroxyapatite nanorods using pyridoxal-5′-phosphate as a phosphorus source, Mater. Res. Bull. 55 (2014) 67–70, http://dx.doi.org/10.1016/j.materresbull.2014.04.008.
[7] C. Qi, Y.-J. Zhu, C.-T. Wu, T.-W. Sun, Y.-Y. Jiang, Y.-G. Zhang, et al., Sonochemical synthesis of hydroxyapatite nanoflowers using creatine phosphate disodium salt as an organic phosphorus source and their application in protein adsorption, RSC Adv. 6 (2016) 9686–9692, http://dx.doi.org/10.1039/C5RA26231C.
[8] F. Chen, Q.-L. Tang, Y.-J. Zhu, K.-W. Wang, M.-L. Zhang, W.-Y. Zhai, et al., Hydroxyapatite nanorods/poly(vinyl pyrolidone) composite nanofibers, arrays and three-dimensional fabrics: electrospun preparation and transformation to hydroxyapatite nanostructures, Acta Biomater. 6 (2010) 3013–3020, http://dx.doi.org/10.1016/j.actbio.2010.02.015.
[9] F. Mohandes, M. Salavati-Niasari, Particle size and shape modification of hydroxyapatite nanostructures synthesized via a complexing agent-assisted route, Mater. Sci. Eng. C Mater. Biol. Appl. 40 (2014) 288–298, http://dx.doi.org/10.1016/j.msec.2014.04.008.
[10] M. Khalid, M. Mujahid, S. Amin, R.S. Rawat, A. Nusair, G.R. Deen, Effect of surfactant and heat treatment on morphology, surface area and crystallinity in hydroxyapatite nanocrystals, Ceram. Int. 39 (2013) 39–50, http://dx.doi.org/10.1016/j.ceramint.2012.05.090.
[11] E. Kramer, J. Podurgiel, M. Wei, Control of hydroxyapatite nanoparticle morphology using wet synthesis techniques: reactant addition rate effects, Mater. Lett. 131 (2014) 145–147, http://dx.doi.org/10.1016/j.matlet.2014.05.105.
[12] M. Sadat-Shojai, M.-T. Khorasani, A. Jamshidi, Hydrothermal processing of hydroxyapatite nanoparticles—A Taguchi experimental design approach, J. Cryst. Growth 361 (2012) 73–84, http://dx.doi.org/10.1016/j.jcrysgro.2012.09.010.
[13] G. Balasundaram, M. Sato, T.J. Webster, Using hydroxyapatite nanoparticles and decreased crystallinity to promote osteoblast adhesion similar to functionalizing with RGD, Biomaterials 27 (2006) 2798–2805, http://dx.doi.org/10.1016/j.biomaterials.2005.12.008.
[14] Y. Liu, Y. Sun, C. Cao, Y. Yang, Y. Wu, D. Ju, et al., Long-term biodistribution in vivo and toxicity of radioactive/magnetic hydroxyapatite nanorods, Biomaterials 35 (2014) 3348–3355, http://dx.doi.org/10.1016/j.biomaterials.2013.12.064.
[15] P. Melnikov, A.R. Teixeira, A. Malzac, M.D.B. Coelho, Gallium-containing hydroxyapatite for potential use in orthopedics, Mater. Chem. Phys. 117 (2009) 86–90, http://dx.doi.org/10.1016/j.matchemphys.2009.05.046.
[16] A. Joseph Nathanael, D. Mangalaraj, S.I. Hong, Y. Masuda, Y.H. Rhee, H.W. Kim, Influence of fluorine substitution on the morphology and structure of hydroxyapatite nanocrystals prepared by hydrothermal method, Mater. Chem. Phys. 137 (2013) 967–976, http://dx.doi.org/10.1016/j.matchemphys.2012.11.010.
[17] K. Zhu, K. Yanagisawa, A. Onda, K. Kajiyoshi, J. Qiu, Morphology variation of cadmium hydroxyapatite synthesized by high temperature mixing method under hydrothermal conditions, Mater. Chem. Phys. 113 (2009) 239–243, http://dx.doi.org/10.1016/j.matchemphys.2008.07.049.
[18] G.S. Kumar, A. Thamizhavel, Y. Yokogawa, S.N. Kalkura, E.K. Girija, Synthesis, characterization and in vitro studies of zinc and carbonate co-substituted nano-hydroxyapatite for biomedical applications, Mater. Chem. Phys. 134 (2012) 1127–1135, http://dx.doi.org/10.1016/j.matchemphys.2012.04.005.
[19] J. Pan, W.-J. Liu, C. Hua, L.-L. Wang, D. Wan, J.-B. Gong, Polymeric nanocomposites loaded with fluoridated hydroxyapatite Ln3+ (Ln = Eu or Tb)/iron oxide for magnetic targeted cellular imaging, Cancer Biol. Med. 12 (2015) 175–183, http://dx.doi.org/10.7497/j.issn.2095-3941.2015.0014.
[20] D. Wan, W. Liu, L. Wang, H. Wang, J. Pan, Fluoridated hydroxyapatite: Eu 3+ nanorods-loaded folate-conjugated D- α -tocopheryl polyethylene glycol succinate (vitamin E TPGS) micelles for targeted imaging of cancer cells, Nanotechnology 27 (2016) 105703, http://dx.doi.org/10.1088/0957-4484/27/10/105703.
[21] M.E. Bartolini, J. Pekar, D.R. Chettle, F. McNeill, A. Scott, J. Sykes, et al., An investigation of the toxicity of gadolinium based MRI contrast agents using neutron activation analysis, Magn. Reson. Imaging 21 (2003) 541–544, http://dx.doi.org/10.1016/S0730-725X(03)00081-X.
[22] L. Cao, B. Li, P. Yi, H. Zhang, J. Dai, B. Tan, et al., The interplay of T1- and T2-relaxation on T1-weighted MRI of hMSCs induced by Gd-DOTA-peptides, Biomaterials 35 (2014) 4168–4174, http://dx.doi.org/10.1016/j.biomaterials.2014.01.073.
[23] J.-A. Park, Y.J. Lee, I.O. Ko, T.-J. Kim, Y. Chang, S.M. Lim, et al., Improved tumor-targeting MRI contrast agents: Gd(DOTA) conjugates of a cycloalkane-based RGD peptide, Biochem. Biophys. Res. Commun. 455 (2014) 246–250, http://dx.doi.org/10.1016/j.bbrc.2014.10.155.
[24] R. Ahmadi, M. Malek, H.R.M. Hosseini, M.A. Shokrgozar, M.A. Oghabian, A. Masoudi, et al., Ultrasonic-assisted synthesis of magnetite based MRI contrast agent using cysteine as the biocapping coating, Mater. Chem. Phys. 131 (2011) 170–177, http://dx.doi.org/10.1016/j.matchemphys.2011.04.083.
[25] O.R. NationalDecay of Gadolinium-159$, vol. 920, 1958, pp. 262–266.
[26] C. Socaci, L. Magerusan, R. Turcu, J. Liebscher, Developing novel strategies for the functionalization of core–shell magnetic nanoparticles with folic acid derivatives, Mater. Chem. Phys. 162 (2015) 131–139, http://dx.doi.org/10.1016/j.matchemphys.2015.05.046.
[27] S.A. Shah, A. Majeed, K. Rashid, S.U. Awan, PEG-coated folic acid-modified superparamagnetic MnFe2O4 nanoparticles for hyperthermia therapy and drug delivery, Mater. Chem. Phys. 138 (2013) 703–708, http://dx.doi.org/10.1016/j.matchemphys.2012.12.044.
[28] R. Yang, E.A. Kolb, J. Qin, A. Chou, R. Sowers, B. Hoang, et al., The folate receptor α is frequently overexpressed in osteosarcoma samples and plays a role in the uptake of the physiologic substrate 5-methyltetrahydrofolate, Clin. Cancer Res. 13 (2007) 2557–2567, http://dx.doi.org/10.1158/1078-0432.CCR-06-1343.
[29] Y. Wan, C. Wu, G. Zuo, G. Xiong, J. Jin, R. Guo, et al., Controlled template synthesis of lamellar hydroxyapatite nanoplates as a potential carrier for gene delivery, Mater. Chem. Phys. 156 (2015) 238–246, http://dx.doi.org/10.1016/j.matchemphys.2015.03.011.
[30] C. Wang, X. Liu, M.E. Fleet, S. Feng, R. Xu, High-pressure synthesis and single-crystal structure refinement of gadolinium holmium silicate hydroxyapatite Gd4.33Ho4.33(SiO4)6(OH)2, J. Solid State Chem. 179 (2006) 2245–2250, http://dx.doi.org/10.1016/j.jssc.2006.03.047.
[31] F. Zeng, J. Wang, Y. Wu, Y. Yu, W. Tang, M. Yin, et al., Preparation of pore expanded mesoporous hydroxyapatite via auxiliary solubilizing template method, Coll. Surf. A Physicochem. Eng. Asp. 441 (2014) 737–743, http://dx.doi.org/10.1016/j.colsurfa.2013.10.028.
[32] J. Pan, D. Wan, Y. Bian, H. Sun, C. Zhang, F. Jin, et al., Fluorescent hydroxyapatite-loaded biodegradable polymer nanoparticles with folate decoration for targeted imaging, AIChE J. 59 (2013) 4494–4501, http://dx.doi.org/10.1002/aic.14210.
[33] E.S. Lee, K. Na, Y.H. Bae, Polymeric micelle for tumor pH and folate-mediated targeting, J. Control. Release (2003) 103–113, http://dx.doi.org/10.1016/S0168-3659(03)00239-6.
[34] I. Hossain, Efficiency and resolution of HPGe and NaI(Tl) detectors using gamma-ray spectroscopy, Sci. Res. Essays 7 (2012) 86–89, http://dx.doi.org/10.5897/SRE11.1717.
[35] A.C. Larson, R.B. Von Dreele, GSAS: General Structural Analysis System, 1994.
[36] A.S. Posner, A. Perloff, A.F. Diorio, Refinement of the hydroxyapatite structure, Acta Crystallogr. 11 (1958) 308–309, http://dx.doi.org/10.1107/S0365110X58000815.
[37] F. Miyaji, Y. Kono, Y. Suyama, Formation and Structure of Zinc-substituted Calcium Hydroxyapatite, vol. 40, 2005, pp. 209–220, http://dx.doi.org/10.1016/j.materresbull.2004.10.020.
[38] J. Kolmas, E. Oledzka, M. Sobczak, G. Na, Nanocrystalline hydroxyapatite doped with selenium oxyanions, A New Mater. Potential Biomed. Appl. 39 (2014) 134–142, http://dx.doi.org/10.1016/j.msec.2014.02.018.
[39] G. Verma, K.C. Barick, N. Manoj, A.K. Sahu, P.A. Hassan, Rod-like micelle templated synthesis of porous hydroxyapatite, Ceram. Int. 39 (2013) 8995–9002, http://dx.doi.org/10.1016/j.ceramint.2013.04.100.
[40] M. Mir, F.L. Leite, P.S. de P. Herrmann Junior, F.L. Pissetti, A.M. Rossi, E.L. Moreira, et al., XRD, AFM, IR and TGA study of nanostructured hydroxyapatite, Mater. Res. 15 (2012) 622–627, http://dx.doi.org/10.1590/S1516-14392012005000069.
[41] S. Choi, S. Coonrod, L. Estroff, C. Fischbach, Chemical and physical properties of carbonated hydroxyapatite affect breast cancer cell behavior, Acta Biomater. 24 (2015) 333–342, http://dx.doi.org/10.1016/j.actbio.2015.06.001.
[42] X. Wu, X. Zhao, Y. Li, T. Yang, X. Yan, K. Wang, In situ synthesis carbonated hydroxyapatite layers on enamel slices with acidic amino acids by a novel two-step method, Mater. Sci. Eng. C 54 (2015) 150–157, http://dx.doi.org/10.1016/j.msec.2015.05.006.
[43] M.F. Cipreste, E.M.B. Sousa, Poly (vinyl alcohol)/collagen/hydroxyapatite nanoparticles hybrid system containing yttrium-90 as a Potential agent to treat osteosarcoma, J. Biomater. Nanobiotechnol. 2014 (2014) 24–30, http://dx.doi.org/10.4236/jbnb.2014.51004.
[44] R.Z. LeGeros, O.R. Trautz, E. Klein, J.P. LeGeros, Two types of carbonate substitution in the apatite structure, Experientia 25 (1969) 5–7. http://www.ncbi.nlm.nih.gov/pubmed/5766584.
[45] E. Iyyappan, P. Wilson, K. Sheela, R. Ramya, Role of triton X-100 and hydrothermal treatment on the morphological features of nanoporous hydroxyapatite nanorods, Mater. Sci. Eng. C 63 (2016) 554–562, http://dx.doi.org/10.1016/j.msec.2016.02.076.
[46] A. Uztetik Morkan, İ. Morkan, S. Demirözü-Şenol, H. Güler, Intermediate products in solid-state reactions of gadolinium oxide and ammonium dihydrogen phosphate, Cryst. Res. Technol. 42 (2007) 1007–1013, http://dx.doi.org/10.1002/crat.200710971.
[47] L.C.M. Pinto, Quantikov Image Analyser, 1996.
[48] J. Chen, Z. Wang, Z. Wen, S. Yang, J. Wang, Q. Zhang, Controllable self-

assembly of mesoporous hydroxyapatite, Coll. Surf. B Biointerf. 127 (2015) 47–53, http://dx.doi.org/10.1016/j.colsurfb.2014.12.055.
[49] F. Chen, P. Huang, Y.J. Zhu, J. Wu, C.L. Zhang, D.X. Cui, The photoluminescence, drug delivery and imaging properties of multifunctional Eu 3+/Gd 3+ dual-doped hydroxyapatite nanorods, Biomaterials 32 (2011) 9031–9039, http://dx.doi.org/10.1016/j.biomaterials.2011.08.032.
[50] R. Liu, C.A. Wang, Synthesis of aluminum-doped mesoporous zirconia with improved thermal stability, Microporous Mesoporous Mater 186 (2014) 1–6, http://dx.doi.org/10.1016/j.micromeso.2013.11.024.
[51] Q. Zheng, H. Yang, J. Wei, J. Tong, Y. Shu, The role and mechanisms of nanoparticles to enhance radiosensitivity in hepatocellular cell, Biomed. Pharmacother. 67 (2013) 569–575, http://dx.doi.org/10.1016/j.biopha.2013.04.003.
[52] J. Bernier, P. Poortmans, Clinical relevance of normal and tumour cell radiosensitivity in BRCA1/BRCA2 mutation carriers: a review, Breast 24 (2015) 100–106, http://dx.doi.org/10.1016/j.breast.2014.12.003.
[53] L.J. Forker, A. Choudhury, A.E. Kiltie, Biomarkers of tumour radiosensitivity and predicting benefit from radiotherapy, Clin. Oncol. 27 (2015) 561–569, http://dx.doi.org/10.1016/j.clon.2015.06.002.
[54] W. Qiang, Q. Wu, F. Zhou, C. Xie, C. Wu, Y. Zhou, Suppression of telomere-binding protein TPP1 resulted in telomere dysfunction and enhanced radiation sensitivity in telomerase-negative osteosarcoma cell line, Biochem. Biophys. Res. Commun. 445 (2014) 363–368, http://dx.doi.org/10.1016/j.bbrc.2014.02.001.
[55] H.S. Hwang, T.W. Davis, J.A. Houghton, T.J. Kinsella, Radiosensitivity of thymidylate synthase-deficient human tumor cells is affected by progression through the G1 restriction point into S-phase: implications for fluoropyrimidine radiosensitization, Cancer Res. 60 (2000) 92–100. http://www.ncbi.nlm.nih.gov/pubmed/10646859.
[56] M.K. Yu, J. Park, S. Jon, Targeting strategies for multifunctional nanoparticles in cancer imaging and therapy, Theranostics 2 (2012) 3–44, http://dx.doi.org/10.7150/thno.3463.
[57] P.P. Mokoena, I.M. Nagpure, V. Kumar, R.E. Kroon, E.J. Olivier, J.H. Neethling, et al., Enhanced UVB emission and analysis of chemical states of Ca5(PO4)3OH: Gd3+,Pr3+ phosphor prepared by co-precipitation, J. Phys. Chem. Solids 75 (2014) 998–1003, http://dx.doi.org/10.1016/j.jpcs.2014.04.015.
[58] W.J. Landis, J.R. Martin, X-ray photoelectron spectroscopy applied to gold-decorated mineral standards of biological interest, J. Vac. Sci. Technol. A Vac. Surf., Film. 2 (1984) 1108, http://dx.doi.org/10.1116/1.572680.
[59] C.D. Wagner, G.E. Muilenberg, Handbook of X-ray Photoelectron Spectroscopy: a Reference Book of Standard Data for Use in X-ray Photoelectron Spectroscopy, Physical Electronics Division, Perkin-Elmer Corp, 1979. https://books.google.com.br/books?id=oY5TAAAAYAAJ.
[60] A. Serret, M.V. Cabañas, M. Vallet-Regi, Stabilization of calcium oxyapatites with lanthanum(III)-created anionic vacancies, Chem. Mater 12 (2000) 3836–3841, http://dx.doi.org/10.1021/cm001117p.
[61] J.F. Cawthray, A.L. Creagh, C.A. Haynes, C. Orvig, Ion exchange in hydroxyapatite with lanthanides, Inorg. Chem. 54 (2015) 1440–1445, http://dx.doi.org/10.1021/ic502425e.
[62] W.P. Cacheris, S.C. Quay, S.M. Rocklage, The relationship between thermodynamics and the toxicity of gadolinium complexes, Magn. Reson. Imaging 8 (1990) 467–481, http://dx.doi.org/10.1016/0730-725X(90)90055-7.
[63] A. Ashokan, D. Menon, S. Nair, M. Koyakutty, A molecular receptor targeted, hydroxyapatite nanocrystal based multi-modal contrast agent, Biomaterials 31 (2010) 2606–2616, http://dx.doi.org/10.1016/j.biomaterials.2009.11.113.
[64] A.A. Moço, Development of Hydroxyapatite-based Nanoparticles for Medical Imaging Diagnosis, Universidade do Porto, 2013.
[65] J.E. Martin, Physics for Radiation Protection, a Handbook, Completely Revised and Enlarged, second ed., WILEY-VCH, Weinheim, 2008, http://uqu.edu.sa/files2/tiny_mce/plugins/filemanager/files/4310166/Physics_for_Radiation_Protection.pdf\npapers2://publication/uuid/C8073439-1A50-43C4-BB86-59182A66831D.